Preprint Title	Local stiffness and work-function variations of hexagonal boron nitride on Cu(111)
Authors	Abhishek Grewal, Yuqi Wang, Matthias Münks, Klaus Kern and Markus Ternes
Publication Date	30 März 2021
Article Type	Letter
ORCID® iDs	Abhishek Grewal - https://orcid.org/0000-0002-4566-8499

Local stiffness and work-function variations of hexagonal boron nitride on Cu(111)

Abhishek Grewal*[1], Yuqi Wang[1,2], Matthias Münks[1], Klaus Kern[1,3] and Markus Ternes*[1,2,4]

Address: [1]Max Planck Institut für Festkörperforschung, Heisenbergstrasse 1, D-70569 Stuttgart, Germany; [2]Peter Grünberg Institute, Forschungszentrum Jülich, D-52425 Jülich, Germany; [3]Institut de Physique, École Polytechnique Fédérale de Lausanne, CH-1015 Lausanne, Switzerland and [4]II. Institute of Physics, RWTH Aachen University, D-52074 Aachen, Germany

Email: Abhishek Grewal - a.grewal@fkf.mpg.de; Markus Ternes - ternes@physik.rwth-aachen.de

* Corresponding author

Abstract

Combined scanning tunnelling and atomic force microscopy using a qPlus sensor enables the measurement of electronic and mechanic properties of two dimensional (2D) materials at the nanoscale. In this work we study hexagonal boron nitride (*h*-BN), an atomically thin 2D layer, that is van der Waals coupled to a Cu(111) surface. The system is of interest as a decoupling layer for functional 2D heterostructures due to the preservation of the *h*-BN bandgap and as a template for atomic and molecular adsorbates owing to its local electronic trapping potential due to in-plane electric field. We obtain work-function (Φ) variations on the *h*-BN/Cu(111) superstructure in the order of 100 meV using two independent methods, namely the shift of field emission resonances (FER) and contact potential difference (CPD) measured by Kelvin probe force microscopy (KPFM). Using 3D force profiles of the same area we determine the relative stiffness of the Moiré region allowing us to analyse both electronic and mechanical properties of the 2D layer simultaneously. We obtain a sheet stiffness of 9.4 ± 0.9 N m^{-1} which is an order of magnitude higher than the one obtained for *h*-BN/Rh(111). Using constant force maps we are able to derive height profiles of

the *h*-BN/Cu(111) showing that the system has a corrugation of 0.6 ± 0.2 Å which helps demystify discussion around the flatness of the *h*-BN/Cu(111) substrate.

Keywords

hexagonal boron nitride; decoupling layers; Moiré superstructure; work-function variation; local stiffness

Introduction

Two-dimensional hexagonal boron nitride (*h*-BN) is among the list of materials that garnered tremendous interest following the exfoliation of mono- and few-layer thick graphene films [1,2]. Unique properties like high thermal stability and conductivity, immense intra-sheet stiffness, and excellent dielectric properties make *h*-BN interesting for technological applications. For example, thin films of *h*-BN have been used as a passivating layer for graphene and MoS_2-based electronics utilising the small lattice mismatch, the large optical phonon modes, and particularly the large bandgap [3-10]. Furthermore, when grown on metal substrates *h*-BN can be used as a nanotemplate for atoms, molecules, and nanostructures with well controlled adsorption and electronic properties [11-18]. In such systems, *h*-BN shows a rich structural and electronic morphology which depends on the lattice mismatch and the interaction strength with the substrate: Large and flat lattice-matched terraces for *h*-BN/Ni(111) [19,20], strain-induced highly-corrugated layers for *h*-BN/Rh(111) [21-23], and template layers for molecules with strong local variations of the work-function for *h*-BN/Ir(111) [24] are representative of such morphological diversity.

We use low-temperature combined scanning tunnelling (STM) and non-contact atomic force microscopy (nc-AFM) to study *h*-BN on Cu(111). This template has interesting properties because the dielectric layer is only very weakly bound to the metal and shows an electronically induced Moiré superstructure [25,26]. First STM studies on this system pointed to only a small geometrical corrugation [27]. Further experimental investigations, using both local probes and averaging techniques, revealed more details of the mechanical and electronic properties of the system, but also inconsistent results about the structural corrugation [26,28-30]. For example, Brülke *et al.* used

high-resolution low energy electron diffraction and normal incidence X-ray standing wave techniques to detect the large separation of 3.24 Å between the *h*-BN sheet and the topmost Cu(111) layer [29]. They found almost no height difference between B and N atoms and excluded significant buckling perpendicular to the surface. Interestingly, this stays in contrast to measurements by Schwarz *et al.* which used a more local analysis of the corrugation by exploiting nc-AFM concluding an absolute height difference of $0.3 - 0.7$ Å between "rim" and "valley" sites of the spatially corrugated monolayer [26]. Recently, however, Zhang *et al.* used STM in combination with DFT simulations to study the variation of the local work-function and bandgap within the Moiré superlattice and found that the variation depends on the angle of the Moiré with respect to the substrate lattice, but inferred only marginal structure modulation [30].

To shed more light on this controversy we use an alternative method to verify the mechanical properties of the monolayer by measuring the stiffness of the *h*-BN layer at different locations of the superstructure and comparing these results with concomitantly recorded local work-function variations. We determine the stiffness of the system by mapping and comparing the short-range interaction forces between the monolayer and the probing metallic tip [31]. This technique enables us to detect the sheet stiffness with unprecedented spatial resolution [23]. On *h*-BN/Rh(111), a different system than studied in this work, the extremely low stiffness of only $\approx 1\ \mathrm{N\,m^{-1}}$ at the weakly bound rim areas confirmed the buckling of the monolayer into the third-dimension to relieve the strain induced by the significant lattice mismatch of this strongly corrugated van der Waals layer [23].

Results and Discussion

STM/AFM on *h*-BN/Cu(111)

As illustrated in Figure 1(a), we employ nc-AFM to probe the electronic and topographic structure of a monolayer of *h*-BN on the Cu(111) surface. Figure 1(b) shows a typical large scale constant-current STM scan of this structure. We observe the monolayer growing over step-edges of the underlying Cu(111) substrate. Weak interlayer interaction allows the van der Waals layer to have varying relative rotational orientations, $\theta \approx 0^\circ - 4^\circ$, on the substrate corresponding to a Moiré pattern

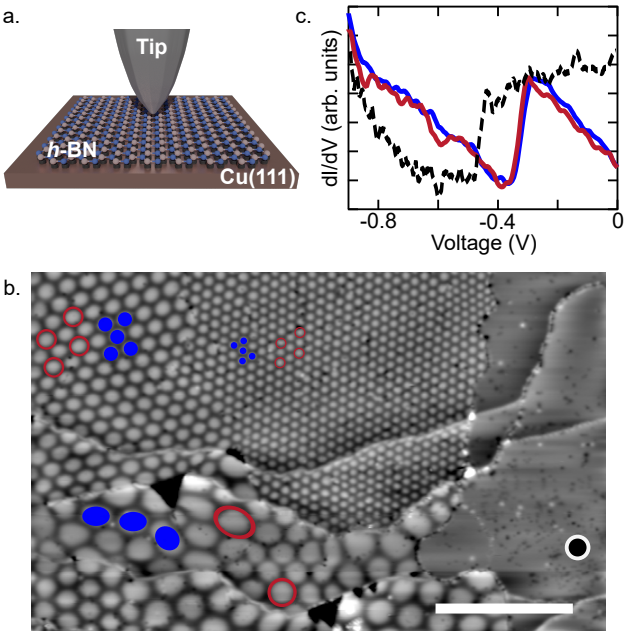

Figure 1: (a.) Scheme of the experiment. (b.) Large scale (200 × 125 nm^2) constant-current (I = 20 pA, V = 3.7 V) STM topography of the h-BN/Cu(111) and bare Cu(111) surface. Blue circles and red rings mark exemplary valley and rim areas, respectively. (c.) Differential conductance dI/dV spectra taken at rim (red line) and valley (blue line) sites and at the bare Cu(111) substrate (dashed black line).

wavelength of $\lambda \approx 3$ nm-14 nm. Furthermore, we observe a shift of the surface state onset of the Cu(111) from ≈ -480 meV on the bare substrate to ≈ -320 meV on the h-BN/Cu(111) (Figure 1(c)) [32]. We found this shift to vary only marginally ($\approx \pm 10$ meV) with the Moiré periodicity or between rim and valley sites [33,34].

h-BN/Cu(111) is known to have an indirect bandgap of 6.1 eV [35] which can be modulated by the Moiré pattern [30]. We analyse the substrate using STM topography, dI/dV, and frequency shift Δf AFM maps at low (in-gap) and high (conduction band onset) bias conditions (see Figure 2). Due to h-BN being insulating, no spectroscopic contribution is expected at low bias voltages making it transparent to STM, as seen in Figure 2(b, d). At this bias only Friedel oscillations due to the scattering of the Cu(111) surface state electrons on defects and adsorbates are observed. Contrarily, as Figure 2(a) reveals, at higher bias the STM topography corresponds to the modulation of the h-BN/Cu(111) interface state as we will show below.

Despite the large change in electronic density of states and thus tip height between the data ob-

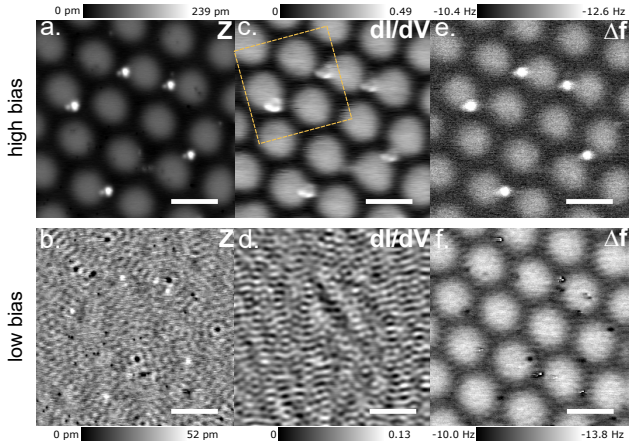

Figure 2: STM/AFM characterisation of *h*-BN/Cu(111) Moiré superstructure. (a., b.) Constant-current topography at $I = 500$ pA and $V = 3.6$ V (top) or $V = 5$ mV (bottom). (c., d.) Simultaneously measured differential conductance (dI/dV) maps ($V_{\mathrm{mod}} = 10$ mV (top) and $V_{\mathrm{mod}} = 1$ mV (bottom), respectively), and (e., f.) frequency shift (Δf) maps ($A_{\mathrm{osc}} = 50$ pm). The dashed yellow box marks the area used for the Φ maps. Scale bar: 10 nm.

tained at the two different sample biases, we observe a one to one correspondence between the simultaneously recorded Δf images and the STM topography. Also, the Δf variation between rim and valley areas in both images changes only marginally. The additionally imaged adsorbates (dot or ring like features) allow thereby the precise alignment between the subsequently acquired data sets.

Work-function variation

While the work-function is generally discussed in the framework of a macroscopic quantity [36], we will use the notation, valid also on the nanoscale, that Φ is the local surface potential measured from the Fermi level, E_F [37]. For a nano-patterned surface, such as *h*-BN/Cu(111), Φ fluctuations can originate from locally varying charge transfer between the substrate and the dielectric layer [38-40].

In our studied substrate, it is the lattice mismatch between the *h*-BN and the Cu(111) substrate, which leads to a varying atomic registry and subsequently induces a lateral modulation of the charge transfer [41]. Additionally, this leads to in-plane electric fields which have been shown to trap atoms, molecules, and nanoclusters [11,13,42].

To map the local Φ fluctuations and to correlate them with the structural properties of the surface, we use two complementary methods: the first method is based on the shift of the FER induced by Φ variations. The effective potential well of depth Φ at the surface of a metal can accommodate a series of Rydberg states, extending a few Å into the vacuum above the metal surface [43]. These image potential states (IPSs) are delocalised in the surface plane and contain the full band of the 2D electron gas. However, the electric field exerted by the proximity of the probing tip distorts the energy spacing of the IPSs and are referred as FER which are revealed in $\mathrm{d}I/\mathrm{d}V$ measurements as strong peaks at positive bias [43]. Figure 3(a) shows such spectra in which we observe a series of peaks whose energies are strongly influenced by the measurement position. The non-trivial double peak structure at approximately $3.5 - 4.5$ V is due to varying contributions from the two interfaces of the dielectric layer. We therefore evaluate the unambiguous shift of the 2nd peak at around $5.6 - 6.0$ V as a measure for the local Φ variation.

Our nc-AFM allows us to employ with KPFM a second, independent method to detect the variation in Φ. For this we record the frequency shift, Δf, of the resonance frequency of the perpendicular to the surface oscillating cantilever versus bias voltage (see Figure 3(b)). At the extrema of the parabolic Δf curves, the electrostatic force is minimised by the applied voltage which compensates the contact potential difference between Φ of tip and Φ of sample [44].

Using the shift of the FER we find an average variation between valley and rim regions of $\Delta\Phi = 148 \pm 17$ meV which agrees well with previous observations [27,45]. Interestingly, however, we find a significantly smaller average difference between valley and rim regions of only $\Delta\Phi = 86 \pm 16$ meV when analysing the CPD data. This hints toward a lower lateral resolution of the KPFM measurement compared to the FER map. The Δf signal in KPFM originates from the relatively long-range electrostatic interaction which is therefore a weighted average over the relevant size of tip (radii $\approx 5 - 10$ nm [46]) that is of same order as the size of the rim and valley regions and, as a result, lead to an underestimation of the $\Delta\Phi$. Nevertheless, both measurement techniques agree well in their qualitative results as it is evident from the $\Delta\Phi$ maps (see Figure 3(b,c)).

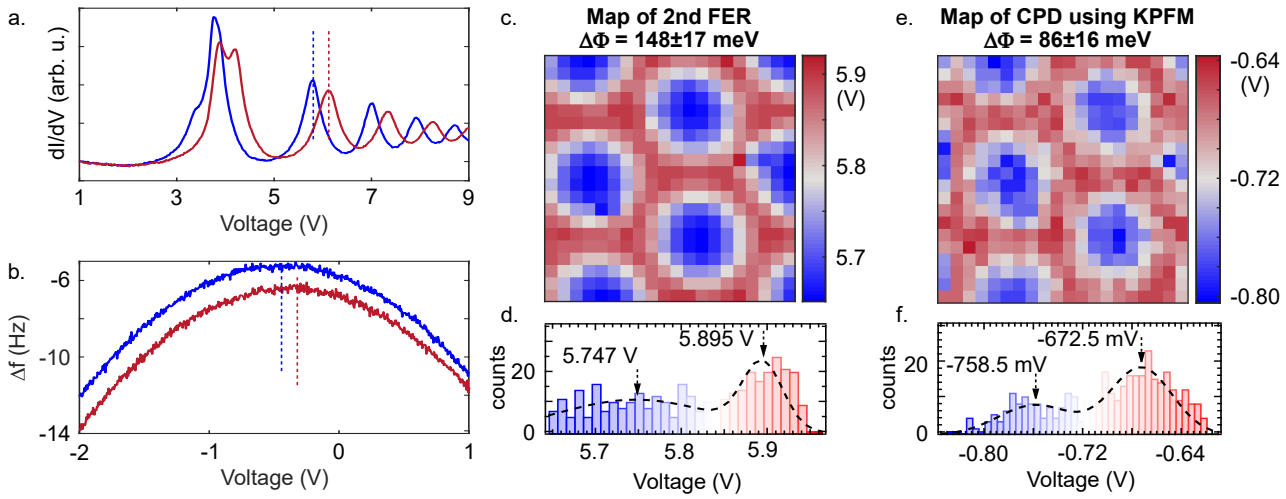

Figure 3: Work-function variation between rim (red) and valley (blue) areas measured using (a.) dI/dV at constant current ($I = 100$ pA) and (b.) KPFM at constant height (stabilised in the valley at $I = 100$ pA, $V = 10$ mV, $A_{\mathrm{mod}} = 50$ pm), respectively. The dotted vertical lines mark exemplary FER and CPD values used for the spatially resolved plots shown in (c.) and (d.). The maps are taken at the yellow box indicated in Figure 2c on a 20×20 grid over 20×20 nm^2. They display the position of the maximum of the second peak in the FER (c.) and the maximum of the KPFM parabola (e.), respectively. (d., f.) Histograms and fits for rim and valley where arrows mark the centre positions of the Gaussians used for the determination of the distribution centre.

Stiffness

Probing the force perpendicular to the substrate, $F_\perp$, at varying tip-sample separations z, the effective stiffness of a nanostructure can be evaluated by comparing the $F_\perp(z)$ behaviour at different areas of the Moiré superstructure [23]. Additionally, such set of data enables us to obtain maps of constant tip-sample interaction forces that allow quantification of the corrugation of Moiré superstructure.

To achieve such data we map the Δf signal at constant oscillation amplitude for an 8×8 nm^2 area at 28 relative tip-surface distances between $z = 0$ and 270 pm. We define $z = 0$ as the tip-sample separation in the valley at $I = 100$ pA and $V = 10$ mV.

Using the matrix inversion method [47] we convert the 3D stack of Δf data into the out-of surface force component $F_\perp$. The now obtained 3D force stack enables us to evaluate the interaction between the tip and the monolayer substrate without being strongly influenced by the electronic corrugation as in STM only measurements. By taking a 2D cut at constant force through the 3D stack,

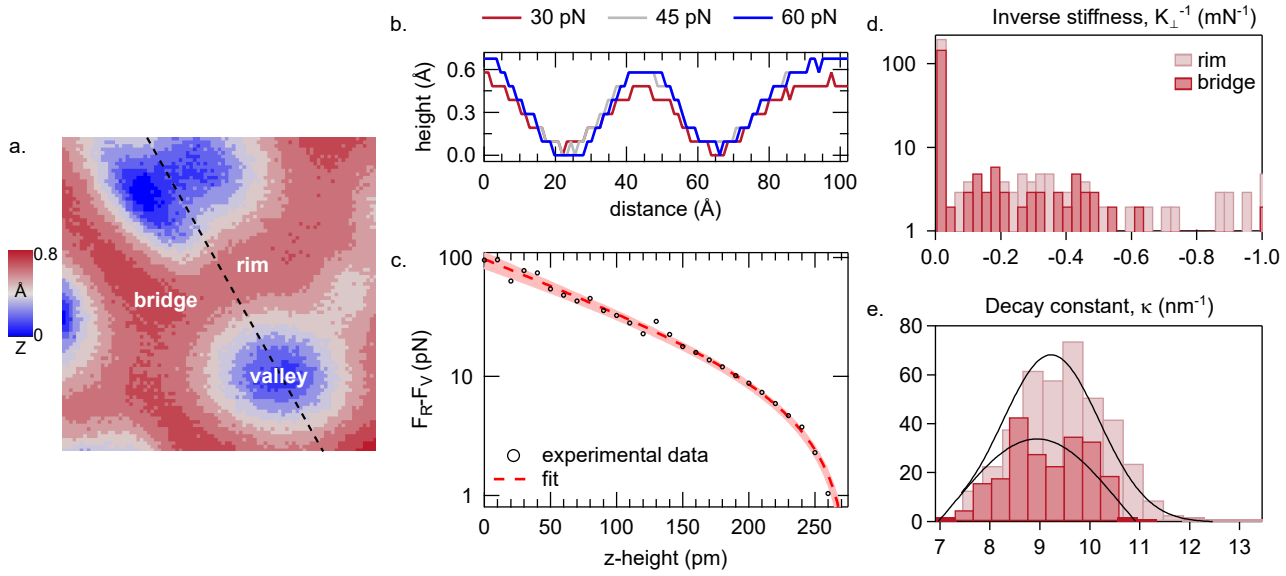

Figure 4: Local stiffness of *h*-BN/Cu(111). (a.) Topography of a 8×8 nm^2 *h*-BN/Cu(111) corresponding to a constant force $F_\perp = 30$ pN. (b.) Line profiles taken from constant vertical force maps along the black dashed line in (a.), at $F_\perp = 30$ pN (red), 45 pN (grey), and 60 pN (blue), respectively. (c.) Average short range force obtained for the rim and the bridge region after subtracting the contribution from valley area (dots) and fit (dashed line). The red area mark the 90% confidence range. (d.,e.) Histograms of inverse stiffness ($K_\perp^{-1}$) and decay constant (κ) of the rim (pink) and bridge sites (red), respectively.

we obtain a topography at a constant tip-substrate interaction force which allows us to visualise the corrugation between rim and valley areas (see Figure 4(a)). Figure 4(b) shows different line profiles corresponding to constant force values of $F_\perp = 30$ pN, 45 pN, and 60 pN. These line profiles reveal an average corrugation of 0.6 ± 0.2 Å which agrees well with the corrugation of $0.3 - 0.7$ Å obtained by Schwarz *et al.* [26]. In these line profiles we obtain a minimal corrugation increase at increased constant force values which hints to some mechanical relaxations of the rim areas under the influence of the force exerted by the tip.

To analyse this effect we separate the short-range forces which act between the tip apex and the sample and which varies over the corrugation of the monolayer, from electrostatic and van der Waals long-range forces by subtracting the average total force F_V measured in the valley areas (blue regions in Fig. 4(a)) from the total forces F_R acting at rim and bridge sites of the superstructure (red regions in Fig. 4(a)). The resulting difference $F_D = F_R - F_V$ is the additional short-range

force which solely influences rim and bridge areas and which might locally lift the *h*-BN layer leading to an increase of corrugation. Figure 4(c) shows the over rim and bridge sites averaged $F_D(z)$ which decays with z mainly exponentially as expected from an interatomic short-range force when neglecting Pauli repulsion [23,48]. The over-exponential decay at $z > 200$ pm is caused by a small offset of $F_0 \approx 1$ pN due to the finite set of Δf data which results in $F_R \equiv F_V$ at the last measurement height ($z = 270$ pm, see Methods). A very soft *h*-BN-layer would show an additional over-exponential increase at small z due to the lifting of the sheet by $\Delta z = F_D(z)K_\perp^{-1}$, where $K_\perp$ is the local vertical stiffness [23]. Assuming an exponential decay of the intrinsic short-range force between tip an substrate and compensating for any lifting, we get for the local vertical force, F_D, as a function of relative height:

$$F_D(z) = (\kappa/K_\perp) \times W_0(F_0\kappa/K_\perp \exp[-\kappa z]) + F_0, \quad (1)$$

where W_0 is the real-valued branch of the Lambert W function and κ is the decay constant [23]. As shown in Figure 4(c) we obtain a good agreement between our data and the model. The best fit yields a local vertical stiffness of $K_\perp = 9.4 \pm 0.9$ N m^{-1} (Figure 4(c)), which demonstrate the high stiffness (negligible softness) of the *h*-BN monolayer on Cu(111) that is an order of magnitude higher than found on Rh(111) [23]. The statistical evaluation of the spatial variation of $K_\perp$ is shown in Figure 4d. The dramatic peak at small inverse stiffness in both rim and bridge areas means an almost perfect exponential behaviour of the short-range force and that $h-\mathrm{BN/Cu(111)}$ undergoes no significant deformation. Also the histogram of the decay constant κ in Figure 4(e) reveal only negligible differences between rim ($\kappa = 9.2 \pm 1.3$ nm^{-1}) and bridge areas ($\kappa = 8.9 \pm 1.4$ nm^{-1}) indicating almost no difference in the mechanical properties between different areas of the Moiré superstructure.

Conclusion

In summary, we report the electronic and mechanical characterisation of *h*-BN/Cu(111) using an STM/AFM. Our STM studies corroborate that the *h*-BN monolayer is only weakly coupled to the Cu(111) surface as is evidenced by the large angular range of Moiré superstructures observed which in turn leads to work-function patterning. Using FER and KPFM maps we report a work-function variation of 148 ± 17 and 86 ± 16 meV, respectively, which agrees well with the previous experimental and theoretical studies [27,45].

3D force maps, obtained by constant height Δf imaging, allow us to test the mechanical stability of the monolayer substrate in the short-range force regime. Using the AFM tip as a nanoindenter we probe its effect on the *h*-BN/Cu(111) system. We obtain a sheet stiffness of $K_\perp = 9.4 \pm 0.9\ \mathrm{N\,m^{-1}}$, which is an order of magnitude larger than that obtained on *h*-BN/Rh(111), indicating substantial mechanical stability. Small lattice mismatch between *h*-BN and Cu(111) as compared to *h*-BN and Rh(111) results in lower strain and no buckling of the substrate leading to high stiffness. Furthermore, our results corroborate that *h*-BN/Cu(111) has a small corrugation of 0.6 ± 0.2 Å but is mechanically stiff making it an appealing platform for studying intrinsic electronic and mechanical properties of nanostructures.

Experimental

We employ a custom-built ultra-high vacuum ($< 10^{-10}$ mbar) low-temperature ($T = 1.4$ K) nc-AFM operated in frequency-modulated mode. A stiff qPlus cantilever design [49] ($k_0 = 1800\ \mathrm{N\,m^{-1}}$, $f_0 = 29077$ Hz, $Q = 60000$) at an oscillation amplitude A = 50 pm enables the nc-AFM functionality [50]. The bias voltage V is applied to the substrate and the tunnelling current I is measured at the virtually grounded tip. The STM/AFM images were processed with the Gwyddion software [51].

FER and KPFM measurements: FER measurements are taken by modulating V ($f_m = 607$ Hz, $V_m = 10$ mV peak-to-peak) and detecting the dI/dV signal with lock-in technique while the tip height is adjusted so that the current I remains constant (constant current mode) during the bias

sweep. For KPFM measurements we stabilise the tip height at $I = 100$ pA and $V = 10$ mV. We then record the frequency shift Δf with respect to f_0 while V is swept at constant tip height.

Vertical stiffness: The 3D Δf data ($8 \times 8 \times 0.27$ nm^3), evaluated in this work, are obtained by taking 28 2D maps at successively increased tip-sample separation ($\Delta z = 10$ pm) stating from a tip height stabilised at $I = 100$ pA, $V = 10$ mV. We use the exponential dependence of average current as the tip is retracted to compensate for z-drift over ≈ 23 h of data acquisition time.

Sample preparation: A Cu(111) single crystal (MaTeck GmbH) is cleaned via repeated cycles of Ar-ion sputtering at room temperature followed by annealing to 1020 K in an ultra-high vacuum preparation chamber. A partial layer of $h-$BN is grown by chemical vapour deposition (CVD) by heating the Cu(111) sample to 980 K and exposing it to 25 L of borazine ($(HBNH)_3$) gas (Katchem spol s.r.o.). h-BN grows in a self-terminating growth process [52]. It is then transferred in-situ to the nc-AFM for characterisation.

Acknowledgements

A. G., M. M., and M. T. acknowledge support from the Collaborative Research Center (SFB) 767 of the German Research Foundation (DFG) for financial support. M. T. acknowledges support by the Heisenberg Program (Grant No. TE 833/2-1) and the Priority Programme (SPP) 2244 of the DFG and Y. W. would like to thank support from Alexander von Humboldt Foundation through a Humboldt Research Fellowship for Postdoctoral Researchers. We would also like to thank W. Auwärter for stimulating discussions.

References

1. Novoselov, K. S.; Geim, A. K.; Morozov, S. V.; Jiang, D.; Zhang, Y.; Dubonos, S. V.; Grigorieva, I. V.; Firsov, A. A. *Science* **2004**, *306* (5696), 666–669. doi:10/bcqksc.

2. Novoselov, K. S.; Mishchenko, A.; Carvalho, A.; Castro Neto, A. H. *Science* **2016**, *353* (6298), . doi:10/f8w86m.

3. Watanabe, K.; Taniguchi, T.; Kanda, H. *Nature Materials* **2004**, *3* (6), 404–409. doi:10.1038/nmat1134.

4. Dean, C. R.; Young, A. F.; Meric, I.; Lee, C.; Wang, L.; Sorgenfrei, S.; Watanabe, K.; Taniguchi, T.; Kim, P.; Shepard, K. L.; Hone, J. *Nature Nanotechnology* **2010**, *5* (10), 722–726. doi:10/fjfcht.

5. Xue, J.; Sanchez-Yamagishi, J.; Bulmash, D.; Jacquod, P.; Deshpande, A.; Watanabe, K.; Taniguchi, T.; Jarillo-Herrero, P.; LeRoy, B. J. *Nature Materials* **2011**, *10* (4), 282–285. doi:10/d4k5vp.

6. Britnell, L.; Gorbachev, R. V.; Jalil, R.; Belle, B. D.; Schedin, F.; Mishchenko, A.; Georgiou, T.; Katsnelson, M. I.; Eaves, L.; Morozov, S. V.; Peres, N. M. R.; Leist, J.; Geim, A. K.; Novoselov, K. S.; Ponomarenko, L. A. *Science* **2012**, *335* (6071), 947–950. doi:10/hqc.

7. Pakdel, A.; Bando, Y.; Golberg, D. *Chemical Society Reviews* **2014**, *43* (3), 934–959. doi:10/gf6bpz.

8. Li, Q.; Zou, X.; Liu, M.; Sun, J.; Gao, Y.; Qi, Y.; Zhou, X.; Yakobson, B. I.; Zhang, Y.; Liu, Z. *Nano Letters* **2015**, *15* (9), 5804–5810. doi:10/f7rnhm.

9. Cui, X.; Lee, G.-H.; Kim, Y. D.; Arefe, G.; Huang, P. Y.; Lee, C.-H.; Chenet, D. A.; Zhang, X.; Wang, L.; Ye, F.; Pizzocchero, F.; Jessen, B. S.; Watanabe, K.; Taniguchi, T.; Muller, D. A.; Low, T.; Kim, P.; Hone, J. *Nature Nanotechnology* **2015**, *10* (6), 534–540. doi:10/gf3chz.

10. Mendelson, N.; Xu, Z.-Q.; Tran, T. T.; Kianinia, M.; Scott, J.; Bradac, C.; Aharonovich, I.; Toth, M. *ACS Nano* **2019**, *13* (3), 3132–3140. doi:10/gfx5zq.

11. Bose, S.; García-García, A. M.; Ugeda, M. M.; Urbina, J. D.; Michaelis, C. H.; Brihuega, I.; Kern, K. *Nature Materials* **2010**, *9* (7), 550–554. doi:10/b49wjp.

12. Kahle, S.; Deng, Z.; Malinowski, N.; Tonnoir, C.; Forment-Aliaga, A.; Thontasen, N.; Rinke, G.; Le, D.; Turkowski, V.; Rahman, T. S.; Rauschenbach, S.; Ternes, M.; Kern, K. *Nano Letters* **2012**, *12* (1), 518–521. doi:10/cqn9hd.

13. Joshi, S.; Bischoff, F.; Koitz, R.; Ecija, D.; Seufert, K.; Seitsonen, A. P.; Hutter, J.; Diller, K.; Urgel, J. I.; Sachdev, H.; Barth, J. V.; Auwärter, W. *ACS Nano* **2014**, *8* (1), 430–442. doi:10/gf3chd.

14. Jacobson, P.; Herden, T.; Muenks, M.; Laskin, G.; Brovko, O.; Stepanyuk, V.; Ternes, M.; Kern, K. *Nature Communications* **2015**, *6*, 8536. doi:10/f7zbpd.

15. Muenks, M.; Jacobson, P.; Ternes, M.; Kern, K. *Nature Communications* **2017**, *8* (1), 14119. doi:10.1038/ncomms14119.

16. Will, M.; Atodiresei, N.; Caciuc, V.; Valerius, P.; Herbig, C.; Michely, T. *ACS Nano* **2018**, *12* (7), 6871–6880. doi:10/gd3jgf.

17. Mehler, A.; Néel, N.; Kröger, J. *The Journal of Physical Chemistry Letters* **2020**, *11* (13), 5204–5211. doi:10.1021/acs.jpclett.0c01320.

18. Riss, A.; Richter, M.; Paz, A. P.; Wang, X.-Y.; Raju, R.; He, Y.; Ducke, J.; Corral, E.; Wuttke, M.; Seufert, K.; Garnica, M.; Rubio, A.; V. Barth, J.; Narita, A.; Müllen, K.; Berger, R.; Feng, X.; Palma, C.-A.; Auwärter, W. *Nature Communications* **2020**, *11* (1), 1490. doi:10.1038/s41467-020-15210-2.

19. Nagashima, A.; Tejima, N.; Gamou, Y.; Kawai, T.; Oshima, C. *Physical Review Letters* **1995**, *75* (21), 3918–3921. doi:10.1103/PhysRevLett.75.3918.

20. Auwärter, W.; Kreutz, T. J.; Greber, T.; Osterwalder, J. *Surface Science* **1999**, *429* (1), 229–236. doi:10/cnztjm.

21. Corso, M.; Auwärter, W.; Muntwiler, M.; Tamai, A.; Greber, T.; Osterwalder, J. *Science* **2004**, *303* (5655), 217–220. doi:10/bk86qd.

22. Berner, S.; Corso, M.; Widmer, R.; Groening, O.; Laskowski, R.; Blaha, P.; Schwarz, K.; Goriachko, A.; Over, H.; Gsell, S.; Schreck, M.; Sachdev, H.; Greber, T.; Osterwalder, J. *Angewandte Chemie International Edition* **2007**, *46* (27), 5115–5119. doi:10/c5fjgc.

23. Herden, T.; Ternes, M.; Kern, K. *Nano Letters* **2014**, *14* (6), 3623–3627. doi:10/f56gqk.

24. Schulz, F.; Drost, R.; Hämäläinen, S. K.; Demonchaux, T.; Seitsonen, A. P.; Liljeroth, P. *Physical Review B* **2014**, *89* (23), 235429. doi:10/gf3chx.

25. Laskowski, R.; Blaha, P.; Schwarz, K. *Physical Review B* **2008**, *78* (4), 045409. doi:10/cg3cfg.

26. Schwarz, M.; Riss, A.; Garnica, M.; Ducke, J.; Deimel, P. S.; Duncan, D. A.; Thakur, P. K.; Lee, T.-L.; Seitsonen, A. P.; Barth, J. V.; Allegretti, F.; Auwärter, W. *ACS Nano* **2017**, *11* (9), 9151–9161. doi:10/gbvhd5.

27. Joshi, S.; Ecija, D.; Koitz, R.; Iannuzzi, M.; Seitsonen, A. P.; Hutter, J.; Sachdev, H.; Vijayaraghavan, S.; Bischoff, F.; Seufert, K.; Barth, J. V.; Auwärter, W. *Nano Letters* **2012**, *12* (11), 5821–5828. doi:10.1021/nl303170m.

28. Siegel, G.; Ciobanu, C. V.; Narayanan, B.; Snure, M.; Badescu, S. C. *Nano Letters* **2017**, *17* (4), 2404–2413. doi:10/f9vwn3.

29. Brülke, C.; Heepenstrick, T.; Humberg, N.; Krieger, I.; Sokolowski, M.; Weiß, S.; Tautz, F. S.; Soubatch, S. *The Journal of Physical Chemistry C* **2017**, *121* (43), 23964–23973. doi:10/gckcn6.

30. Zhang, Q.; Yu, J.; Ebert, P.; Zhang, C.; Pan, C.-R.; Chou, M.-Y.; Shih, C.-K.; Zeng, C.; Yuan, S. *ACS Nano* **2018**, *12* (9), 9355–9362. doi:10.1021/acsnano.8b04444.

31. Baykara, M. Z.; Schwarz, U. D. 3D Force Field Spectroscopy. In *Noncontact Atomic Force Microscopy: Volume 3*; Morita, S., Giessibl, F. J., Meyer, E., Wiesendanger, R., Eds.; NanoScience and Technology; Springer International Publishing: Cham, 2015; pp 9–28. doi:10.1007/978-3-319-15588-3_2.

298 32. Crommie, M. F.; Lutz, C. P.; Eigler, D. M. *Nature* **1993**, *363* (6429), 524–527. doi:10.1038/
299 363524a0.

300 33. De Renzi, V.; Rousseau, R.; Marchetto, D.; Biagi, R.; Scandolo, S.; del Pennino, U. *Physical*
301 *Review Letters* **2005**, *95* (4), 046804. doi:10/ch4bc5.

302 34. Ziroff, J.; Gold, P.; Bendounan, A.; Forster, F.; Reinert, F. *Surface Science* **2009**, *603* (2),
303 354–358. doi:10/dcg2kf.

304 35. Cassabois, G.; Valvin, P.; Gil, B. *Nature Photonics* **2016**, *10* (4), 262–266. doi:10.1038/
305 nphoton.2015.277.

306 36. Kittel, C.; McEuen, P.; Sons, J. W. . *Introduction to Solid State Physics*; John Wiley & Sons,
307 Limited, 2018.

308 37. Wandelt, K. *Applied Surface Science* **1997**, *111*, 1–10. doi:10.1016/S0169-4332(96)00692-7.

309 38. Ploigt, H.-C.; Brun, C.; Pivetta, M.; Patthey, F.; Schneider, W.-D. *Physical Review B* **2007**, *76*
310 (19), 195404. doi:10/fknqpt.

311 39. Ruffieux, P.; Aït-Mansour, K.; Bendounan, A.; Fasel, R.; Patthey, L.; Gröning, P.; Gröning, O.
312 *Physical Review Letters* **2009**, *102* (8), 086807. doi:10/bhqpbw.

313 40. Borca, B.; Barja, S.; Garnica, M.; Sánchez-Portal, D.; Silkin, V. M.; Chulkov, E. V.; Her-
314 manns, C. F.; Hinarejos, J. J.; Vázquez de Parga, A. L.; Arnau, A.; Echenique, P. M.; Mi-
315 randa, R. *Physical Review Letters* **2010**, *105* (3), 036804. doi:10/fbf2xf.

316 41. Bokdam, M.; Brocks, G.; Katsnelson, M. I.; Kelly, P. J. *Physical Review B* **2014**, *90* (8),
317 085415. doi:10/gf6bp2.

318 42. N'Diaye, A. T.; Bleikamp, S.; Feibelman, P. J.; Michely, T. *Physical Review Letters* **2006**, *97*
319 (21), 215501. doi:10.1103/PhysRevLett.97.215501.

320 43. Gundlach, K. H. *Solid-State Electronics* **1966**, *9* (10), 949–957. doi:10.1016/0038-1101(66)
321 90071-2.

322 44. Melitz, W.; Shen, J.; Kummel, A. C.; Lee, S. *Surface Science Reports* **2011**, *66* (1), 1–27.
323 doi:10/dpzdck.

324 45. Gómez Díaz, J.; Ding, Y.; Koitz, R.; Seitsonen, A. P.; Iannuzzi, M.; Hutter, J. *Theoretical*
325 *Chemistry Accounts* **2013**, *132* (4), 1350. doi:10.1007/s00214-013-1350-z.

326 46. Zerweck, U.; Loppacher, C.; Otto, T.; Grafström, S.; Eng, L. M. *Physical Review B* **2005**, *71*
327 (12), 125424. doi:10/b572bs.

328 47. Giessibl, F. J. *Applied Physics Letters* **2000**, *78* (1), 123–125. doi:10.1063/1.1335546.

329 48. Ternes, M.; Gonzalez, C.; Lutz, C. P.; Hapala, P.; Giessibl, F. J.; Jelinek, P.; Heinrich, A. J.
330 *Phys. Rev. Lett.* **2011**, *106*, 016802.

331 49. Giessibl, F. J.; Hembacher, S.; Herz, M.; Schiller, C.; Mannhart, J. *Nanotechnology* **2004**, *15*
332 (2), S79. doi:10/c4phmm.

333 50. Münks, M. Scanning Tunneling Microscopy and Atomic Force Microscopy Measurements on
334 Correlated Systems. Ph. D. Thesis, Universität Konstanz: Konstanz, 2017.

335 51. Nečas, D.; Klapetek, P. *Open Physics* **2011**, *10* (1), 181–188. doi:10/bjn3cr.

336 52. Nagashima, A.; Tejima, N.; Gamou, Y.; Kawai, T.; Oshima, C. *Physical Review Letters* **1995**,
337 *75* (21), 3918–3921. doi:10.1103/PhysRevLett.75.3918.